Nuclear Science and Techniques (2026) 37:48
https://doi.org/10.1007/s41365-025-01868-0

Superconducting solenoid optimization and field measurements

Shuai Ma[1] · Andre Arnold[2] · Peter Michel[2] · Petr Murcek[2] · Anton Ryzhov[2] · Jana Schaber[2] · J. Teichert[2] · Rong Xiang[2]

Received: 10 November 2024 / Revised: 22 March 2025 / Accepted: 26 March 2025 / Published online: 10 January 2026

Abstract
A solenoid is typically used in normally conducting and superconducting radio frequency (SRF) photoinjectors to compensate for the projected transverse beam emittance. In the ELBE SRF Gun-II, a superconducting solenoid is positioned inside the gun cryomodule approximately 0.7 m from the end of the gun cavity. The spherical aberration and multipole field effects caused by offset and tilt limit the reduction in beam emittance for high bunch charges. We designed a novel superconducting (SC) solenoid with a lower spherical aberration coefficient. In the simulation, the beam emittance from the spherical aberration decreased by 47%. Both the longitudinal and transverse fields were measured and analyzed using the formalism fitting method to assess the performance of the SC solenoid within the cryomodule and its influence on the beam transverse emittance.

Keywords Superconducting solenoid · Magnetic field · Photoinjector · SRF gun

1 Introduction

Over the past decade, a superconducting radiofrequency (SRF) electron source has demonstrated the capability to produce high-quality electron beams, specifically for the "Electron Linac for Beams with High Brilliance and Low Emittance (ELBE)", which is a user facility that generates secondary radiation for a wide range of applications [1–3]. The SRF gun, which primarily operates in continuous wave mode at repetition rates of 50 and 100 kHz, has been instrumental in producing terahertz radiation between 0.2 and 1.5 THz, which is characterized by high pulse energy and significant average power. Equipped with a 3.5-cell niobium cavity resonating at 1.3 GHz, the SRF gun achieves an acceleration gradient of 8 MV/m, corresponding to an on-axis peak electric field of 20.5 MV/m. The SRF gun can deliver electron bunches with up to 300 pC bunch charge utilizing either magnesium (Mg) or cesium telluride (Cs_2Te) cathodes in conjunction with a 262 nm laser [4–10]. This technology shows significant promise for applications in neutron time-of-flight experiments, high-repetition-rate ultrafast electron diffraction, high-power terahertz experiments, and Thomson backscattering experiments that require high bunch charge and repetition rates [11–14].

To control the electron beam size and compensate for projected transverse emittance, a superconducting (SC) solenoid is installed 0.7 m downstream from the cavity end within the SRF gun cryomodule [15, 16]. This distance represents a balanced compromise between the need for magnetic field shielding of the cavity and minimizing the beam emittance. However, a solenoid introduces a new source of emittance owing to spherical aberration, which is linear with respect to the spherical aberration coefficient and scales with the fourth power of the beam RMS size [17]. The spherical aberrations of the solenoid can significantly increase emittance for beams with relatively large diameters [18]. Additionally, measurements indicate that beam aberrations increase with higher solenoid currents, primarily owing to multipole magnetic field effects arising from the tilt and offset position errors of the solenoid [19, 20]. This configuration imposes limitations on applications such as X-ray free-electron laser facilities, which require a lower emittance and higher bunch charge [21–23].

✉ Shuai Ma
ms369@mail.ustc.edu.cn

✉ J. Teichert
j.teichert@hzdr.de

[1] National Key Laboratory of Science and Technology on Advanced Laser and High Power Microwave, Institute of Applied Electronics, China Academy of Engineering Physics, Mianyang 621900, China

[2] Helmholtz-Zentrum Dresden-Rossendorf, 01328 Dresden, Germany

The current SRF gun in operation at ELBE (SRF Gun-II) is part of a developmental progression in SRF gun research and development, which will soon advance to the third-generation SRF Gun-III [24, 25]. The primary objectives of this new generation are to increase the available bunch charge for terahertz production and reduce the transverse emittance through enhanced emittance compensation, correction of multipole magnetic field effects, and mitigation of solenoid aberrations. A newly redesigned solenoid was constructed to achieve these goals. Upon completion of the SRF Gun-III cryomodule, magnetic field measurements were taken to evaluate the performance of the new solenoid. A formalism fitting method was employed to analyze the multipole fields, and the associated measurement errors were quantified. We also assessed the impact of these fields on the beam emittance. The second section of this paper describes the basic concept and field measurement method. The influence of the multipole components, such as the quadrupole and sextupole, is analyzed in this section. A comparison of the new and old designs of SC solenoids is presented in the third section. The fourth section presents the results of the field and error analyses. The fifth section analyzes the influence of the multipole fields on the beam transverse emittance and solutions. The conclusions are presented in the final section.

2 Basic principle

2.1 Spherical aberration of solenoid

Magnetic lenses can exhibit imaging errors, even when the momentum distribution of the particles is negligible. These errors arise because of spherical aberrations that occur as a result of nonlinear magnetic field regions within the lens and particle rays that deviate from the paraxial approximation. Spherical aberration is dependent on the third power of the radial position of the particle within the solenoid and can be represented using two distinct integral expressions [17]:

$$C_s = \frac{1}{2}\frac{\int B(z)'^2 \mathrm{d}z}{\int B(z)^2 \mathrm{d}z}. \tag{1}$$

The transverse emittance resulting from solenoid spherical aberration can be calculated as

$$\varepsilon_{\mathrm{sph}} = \frac{r_0^4}{2\sqrt{6}f}\sqrt{\frac{C_1^2}{12} + \frac{C_1 C_2}{5}r_0^2 + \frac{C_2^2}{8}r_0^4}, \tag{2}$$

$$\begin{aligned} C_1 &= C_s \\ C_2 &= \frac{5}{64}\frac{\int B(z)''^2 \mathrm{d}z}{\int B(z)^2 \mathrm{d}z}. \end{aligned} \tag{3}$$

On the right side of Eq. 2, the higher-order terms are significantly smaller than the leading term. Thus, the spherical aberration emittance scales with the fourth power of the beam RMS size at the solenoid entrance. In high-bunch-charge and short-bunch-length injectors, the beam RMS size is typically large, which amplifies the effect of spherical aberrations. Therefore, decreasing the spherical aberration coefficient is crucial to mitigate its effect on beam quality. As indicated by Eq. 1, reducing the spherical aberration coefficient requires minimizing the integral of the first derivative of the solenoid field at the same field integral.

2.2 Solenoid axis and multipole field measurement

The pulsed wire method is a basic method for analyzing the alignment of magnets [26]. In this method, a wire is fixed between two points using an external field. A current pulse is applied to the wire. If the external field has a transverse component, the local wire will move owing to the Lorentz force, which will propagate to two endpoints as traveling waves and be measured by motion sensors. The amplitude of the motion is related to the transverse magnetic field integration along the z-direction and pulse current magnitude. The axis of the external field can be obtained within 100 μm resolution by analyzing the motions. For solenoids, the other method uses the properties of the solenoid field, in which the longitudinal component on the axis is the extremum along the radial direction and the radial component is zero, as follows:

$$\begin{aligned} \frac{\partial B_z(r,z)}{\partial r} &= 0, \\ B_r(0,z) &= 0. \end{aligned} \tag{4}$$

This method has a worse resolution than the pulsed wire but is concise for the SC solenoid. This is because only one end face of the tube is open in the cryomodule and constructing the wire is challenging.

An important method for analyzing the multipole magnetic field for multipole component measurement is the harmonic coils and wires approach, which was developed by Carlo et al. at CERN LHC [27, 28]. The basic concept relies on Faraday's law of induction; as the magnetic field changes, it induces an electromotive force in the coils, enabling accurate determination of the multipole field components. The Fourier coefficients of the magnetic flux function correspond to the strengths of the multipole components of the field.

Although this method provides highly accurate field measurements, it requires a multifaceted control system and advanced electrical analysis tools. This approach is impractical for accelerator facilities that do not have access to dedicated field measurement laboratories. To streamline the measurement of multipole modes without specialized equipment, we use a 2D polynomial fitting technique based on data obtained from 3D Hall probe measurements. Drawing on the definitions of the dipole, quadrupole, and sextupole components outlined in [29], we proceed with the following approach:

$$\begin{aligned}
\mathbf{B}_{\mathrm{dn}} &= 0\mathbf{e}_{\mathbf{x}} + J_{\mathrm{dn}}\mathbf{e}_{\mathbf{y}},\\
\mathbf{B}_{\mathrm{ds}} &= -J_{\mathrm{ds}}\mathbf{e}_{\mathbf{x}} + 0\mathbf{e}_{\mathbf{y}},\\
\mathbf{B}_{\mathrm{qn}} &= J_{\mathrm{qn}}y\mathbf{e}_{\mathbf{x}} + J_{\mathrm{qn}}x\mathbf{e}_{\mathbf{y}},\\
\mathbf{B}_{\mathrm{qs}} &= -J_{\mathrm{qs}}x\mathbf{e}_{\mathbf{x}} + J_{\mathrm{qs}}y\mathbf{e}_{\mathbf{y}},\\
\mathbf{B}_{\mathrm{sn}} &= J_{\mathrm{sn}}xy\mathbf{e}_{\mathbf{x}} + \frac{1}{2}J_{\mathrm{sn}}(x^2-y^2)\mathbf{e}_{\mathbf{y}},\\
\mathbf{B}_{\mathrm{ss}} &= -\frac{1}{2}J_{\mathrm{ss}}(x^2-y^2)\mathbf{e}_{\mathbf{x}} + J_{\mathrm{ss}}xy\mathbf{e}_{\mathbf{y}},
\end{aligned} \tag{5}$$

where the field coefficients are denoted by J. The subscripts "d", "q", and "s" denote the dipole, quadrupole, and sextupole parts, respectively, whereas "n" and "s" specify whether the mode is of the normal or skew type. In the case of solenoids, the transverse magnetic field can be expressed as

$$\mathbf{B}_{\mathrm{t}} = J_{\mathrm{t}}x\mathbf{e}_{\mathbf{x}} + J_{\mathrm{t}}y\mathbf{e}_{\mathbf{y}}. \tag{6}$$

Thus, the horizontal and vertical fields can be expressed as

$$\begin{aligned}
B_x &= -J_{\mathrm{ds}} + J_{\mathrm{qn}}y + (J_{\mathrm{t}} - J_{\mathrm{qs}})x + \\
&\quad J_{\mathrm{sn}}xy - \frac{1}{2}J_{\mathrm{ss}}(x^2-y^2) + \ldots,\\
B_y &= J_{\mathrm{dn}} + J_{\mathrm{qn}}x + (J_{\mathrm{t}} + J_{\mathrm{qs}})y + \\
&\quad \frac{1}{2}J_{\mathrm{sn}}(x^2-y^2) + J_{\mathrm{ss}}xy + \ldots.
\end{aligned} \tag{7}$$

The Hall effect sensor can accurately measure the horizontal and vertical components of the transverse magnetic field. The coefficients for various multipole modes (e.g., quadrupole and sextupole) can then be derived by applying a numerical fitting algorithm to the functions provided in Eq. 7.

2.3 Influence of multipole fields on beam transverse emittance

The multipole fields resulting from misalignment and manufacturing errors in the solenoid can affect the beam shape and emittance. Because the dipole field components primarily cause beam deflection, we focus on the effects of the quadrupole and sextupole components. Details on the influence of these fields and the methods for their correction can be found in [30].

The 4D phase–space transport matrix for an ideal quadrupole lens under the thin-lens approximation followed by a solenoid lens can be expressed as follows:

$$\mathrm{M}_{\mathrm{sol}}\,\mathrm{M}_{\mathrm{quad}} = \begin{pmatrix}
\cos^2 KL_{\mathrm{s}} & \frac{\sin KL_{\mathrm{s}}\cos KL_{\mathrm{s}}}{K} & \sin KL_{\mathrm{s}}\cos KL_{\mathrm{s}} & \frac{\sin^2 KL_{\mathrm{s}}}{K}\\
-K\sin KL_{\mathrm{s}}\cos KL_{\mathrm{s}} & \cos^2 KL_{\mathrm{s}} & -K\sin^2 KL_{\mathrm{s}} & \sin KL_{\mathrm{s}}\cos KL_{\mathrm{s}}\\
-\sin KL_{\mathrm{s}}\cos KL_{\mathrm{s}} & -\frac{\sin^2 KL_{\mathrm{s}}}{K} & \cos^2 KL_{\mathrm{s}} & \frac{\sin KL_{\mathrm{s}}\cos KL_{\mathrm{s}}}{K}\\
K\sin^2 KL_{\mathrm{s}} & -\sin KL_{\mathrm{s}}\cos KL_{\mathrm{s}} & -K\sin KL_{\mathrm{s}}\cos KL_{\mathrm{s}} & \cos^2 KL_{\mathrm{s}}
\end{pmatrix}\begin{pmatrix}
1 & 0 & 0 & 0\\
-\frac{1}{f} & 1 & 0 & 0\\
0 & 0 & 1 & 0\\
0 & 0 & +\frac{1}{f} & 1
\end{pmatrix}. \tag{8}$$

Here, L_{s} represents the effective length of the solenoid, defined as $\frac{\int B(z)^2\mathrm{d}z}{B_{\mathrm{s}}^2}$, where $B(z)$ is the longitudinal magnetic field as a function of the position z and B_{s} is the peak magnetic field along the solenoid axis. The parameter $K = \frac{eB_0}{2mc\gamma\beta}$, e is the electron charge, m is the electron mass, c is the speed of light, γ is the relativistic factor, and $\beta = v/c$ is the normalized velocity of the particle.

A normal quadrupole lens positioned at the entrance of the solenoid provides focus with a focal length f. After the beam passes through the normal quadrupole and solenoid, the resulting beam matrix takes the following form:

$$\sigma(s) = \mathrm{M}_{\mathrm{sol}}\mathrm{M}_{\mathrm{quad}}\sigma(0)\left(\mathrm{M}_{\mathrm{sol}}\mathrm{M}_{\mathrm{quad}}\right)^{\mathrm{T}}. \tag{9}$$

The additional transverse emittance resulting from the combined effects of the quadrupole focus and solenoid coupling between transverse planes is expressed as

$$\varepsilon_{\mathrm{n,\,quad+sol}} = \beta\gamma\frac{\sigma_{x,\,\mathrm{sol}}\,\sigma_{y,\,\mathrm{sol}}}{f}|\sin 2KL_{\mathrm{s}}|. \tag{10}$$

Here, ε_{n} is the beam-normalized emittance. If the quadrupole field has a rotating angle α_1, the resulting transfer matrix incorporates cross-plane coupling terms between the x- and y-directions and is expressed as

$$\mathrm{M}_{\mathrm{rotquad}}(\alpha_1, f) = \begin{pmatrix}
1 & 0 & 0 & 0\\
\frac{-\cos 2\alpha_1}{f} & 1 & \frac{-\sin 2\alpha_1}{f} & 0\\
0 & 0 & 1 & 0\\
\frac{-\sin 2\alpha_1}{f} & 0 & \frac{\cos 2\alpha_1}{f} & 1
\end{pmatrix}, \tag{11}$$

and Eq. 10 changes to

$$\varepsilon_{\mathrm{n,\,quad+sol}} = \beta\gamma\frac{\sigma_{x,\,\mathrm{sol}}\,\sigma_{y,\,\mathrm{sol}}}{f}|\sin 2(KL_{\mathrm{s}} + \alpha_1)|. \tag{12}$$

To mitigate the emittance growth caused by the quadrupole component parasiting the solenoid, a pair of correction quadrupoles consisting of a normal and skew quadrupole are installed downstream of the solenoid at a distance L. These quadrupoles work together and have a rotation angle α_2,

$$\begin{aligned}
\varepsilon_{n,\mathrm{total}} = \beta\gamma\Bigg|&\frac{\sigma_{x,\mathrm{sol}}\sigma_{y,\mathrm{sol}}}{f}\sin 2\left(KL_{\mathrm{s}} + \alpha_1\right)\\
&+\frac{\sigma_{x,\mathrm{cor}}\sigma_{y,\mathrm{cor}}}{f_{\mathrm{cor}}}\sin(2\alpha_2)\Bigg|.
\end{aligned} \tag{13}$$

Equation 13 demonstrates that the effectiveness of the corrector is strongly dependent on the beam RMS size at the corrector position. In practical applications, the distance between the solenoid and corrector is a key parameter. In the SRF gun configuration, the corrector is positioned 0.437 m downstream of the solenoid, directly outside the cryomodule. Using ASTRA, a beam dynamics simulation tool [31], we performed simulations and compared the results with the theoretical predictions yielded by Eqs. 12 and 13. Figure 1 presents the simulation results for different distances. The simulations revealed that, when the distance parameters were fixed, the insufficient corrector focal strength failed to counteract the quadrupole field from the solenoid properly. This indicates that, for identical parasitic quadrupole strengths in both the solenoid and corrector, shorter distances result in more effective emittance compensation. However, if the distance is too long, as shown by the 0.7 m case (blue line) in Fig. 1, the corrector either fails to cancel the quadrupole field of the solenoid or requires a significantly stronger focal strength to achieve the same effect.

According to Eq. 13, the beam size at the corrector is always smaller than that at the solenoid because the solenoid focuses the beam, and the corrector is positioned within the focal length of the solenoid. Theoretically, if the corrector is placed beyond the focal length of the solenoid, where the beam RMS size is equal to or exceeds that at the solenoid, the emittance compensation improves for a given quadrupole strength. However, because the focal length of the solenoid varies depending on the specific operational parameters, the corrector cannot compensate for the emittance growth that occurs between the solenoid and corrector. Therefore, to achieve optimal emittance compensation, the corrector should be positioned as close as possible to the solenoid.

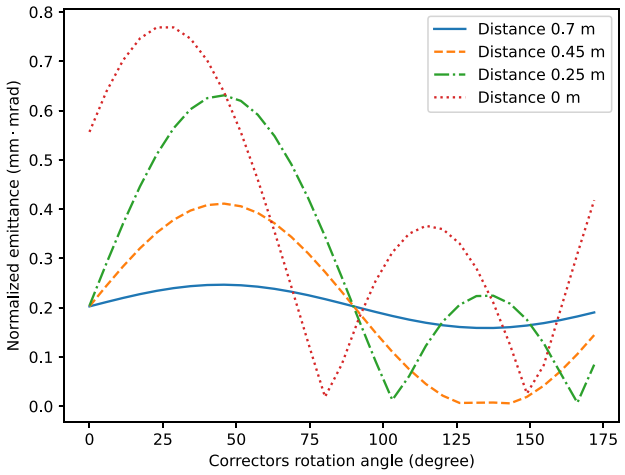

Fig. 1 (Color online) Transverse beam emittance was evaluated using ASTRA simulations. The system comprised a quadrupole magnet integrated with a solenoid, where the quadrupole had an effective length of 0.04 m, a strength of 0.5m^{-2}, and was rotated by 23 degrees relative to the solenoid principal axis. The beam had a kinetic energy of 4 MeV. The solenoid had a maximum magnetic field of 0.171 T, characterized by an effective length (L_s) of 0.04 m. Additionally, a corrector magnet with an effective length of 62.7 mm and a focal length of 16 m was positioned downstream to adjust the beam dynamics

As discussed in [32, 33], the sextupole component can introduce additional transverse emittance to the beam, which is primarily dependent on the radial second-order derivative of the magnetic field and effective length of the field region. To simplify the analysis of sextupole effects, we assume that fringe fields are negligible, which is a valid assumption in this context because fringe effects are minor compared to the main field. Additionally, we consider a paraxial approximation in which the transverse momentum of the beam is much smaller than its longitudinal momentum. Under these conditions, the Lorentz force equation yields the force in the x-direction as follows:

$$F_x = \frac{\mathrm{d}p_x}{\mathrm{d}t} = e\left(v_y B_z - v_z B_y\right). \tag{14}$$

Considering that $\mathrm{d}z = \beta c \mathrm{d}t$, the force becomes

$$\frac{\mathrm{d}p_x}{\mathrm{d}z} = -eB_y. \tag{15}$$

The y-component of the sextupole field is given by [29].

$$B_y(x,y) = \frac{1}{2}\frac{\partial^2 B_y}{\partial x^2}\bigg|_{x,y=0}\left(x^2 - y^2\right). \tag{16}$$

The sextupole field introduces transverse momentum, as follows:

$$\begin{aligned}\int_{p_x}^{p_x+\Delta p_x} \mathrm{d}p_x = \Delta p_x &= -\frac{e}{2}\int_{-\infty}^{\infty}\frac{\partial^2 B_y}{\partial x^2}\bigg|_{x,y=0}\left(x^2 - y^2\right)\mathrm{d}z,\\ \Delta p_x(x,y) &= -\frac{e}{2}\frac{\partial^2 B_y}{\partial x^2}\bigg|_{x,y=0} L_{\mathrm{eff}}\left(x^2 - y^2\right).\end{aligned} \tag{17}$$

The beam emittance is

$$\varepsilon_{\mathrm{n}} = \frac{\sigma_x \sigma_{p_x}}{mc}, \tag{18}$$

where σ_x and σ_{px} are the RMS size and horizontal momentum of the beam, respectively:

$$\sigma_{p_x}^2 = \frac{\int_{-\infty}^{\infty}\left[\Delta p_x(x, y=0)\right]^2 \rho(x)\mathrm{d}x}{\int_{-\infty}^{\infty}\rho(x)\mathrm{d}x}, \tag{19}$$

$\rho(x)$ denotes the transverse beam distribution. For example, $\rho(x)$ may take the form of a Gaussian distribution $e^{-\frac{x^2}{2\sigma_x^2}}$, where σ_x is the beam RMS width, or a uniform distribution. The distribution function influences the extent to which the sextupole component contributes to the emittance growth,

as the nonlinear components of the field interact with the particle density profile in different manners, depending on the distribution. The resulting normalized emittance induced by the sextupole field for both the Gaussian and uniform beam distributions is expressed as

$$\begin{aligned}\varepsilon_{\text{n, sextupole}} &= \frac{\sqrt{3}}{2}\sigma_x^3 \frac{e}{mc} L_{\text{eff}} \left.\frac{\partial^2 B_y}{\partial x^2}\right|_{x,y=0}, \\ \varepsilon_{\text{n, sextupole}} &= \frac{1}{2}\sigma_x^3 \frac{e}{mc} L_{\text{eff}} \left.\frac{\partial^2 B_y}{\partial x^2}\right|_{x,y=0}.\end{aligned} \tag{20}$$

From Eq. 20, the increasing transverse emittance from the parasitic sextupole component is linear with respect to the effective length of the sextupole component and cubic with respect to the beam RMS size. This indicates that larger beam sizes or stronger sextupole components can significantly increase the emittance. To mitigate this effect, a compensating sextupole lens must be inserted near the solenoid. This compensator can counteract the influence of the sextupole component by introducing an opposing sextupole field component. Additionally, reducing the second-order derivative of the transverse magnetic field in the solenoid can help to diminish the sextupole component effect because a smaller second-order derivative reduces the strength of the nonlinear component that contributes to emittance growth.

3 Novel design of SC solenoid

To reduce spherical aberration, we optimized the design of the SC solenoid. Magnetic field calculations were performed using Poisson/Superfish, which is widely used to simulate electromagnetic fields in accelerator components [34]. The results of these calculations are shown in Fig. 2. The NbTi wire coils remained unchanged in both designs, whereas the pure iron yoke was optimized by increasing its radius from $R_1 = 31.75$ mm to $R_2 = 38$ mm and doubling its length from $L_1 = 58.6$ mm to $L_2 = 120$ mm. This optimization significantly altered the magnetic field profile of the solenoid. The normalized longitudinal field and its first derivative for both designs are shown in Fig. 3, where the new design exhibited a substantial reduction in the first derivative at the solenoid field edges. The effective length of the solenoid increased from 40.56 mm to 52.27 mm in the new design.

We conducted simulations using ASTRA to compare the beam dynamics of the old and new solenoid designs. In these simulations, the beam kinetic energy was set to 3.5 MeV and the space charge effect was neglected to focus on the impact of the solenoid on the beam. At the solenoid

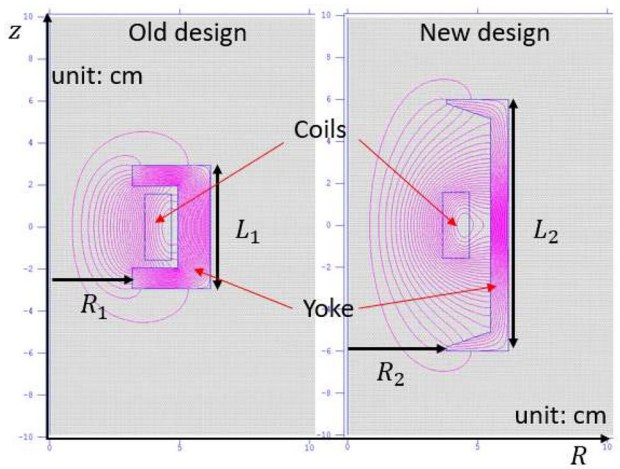

Fig. 2 (Color online) Magnetic field simulation in Poisson Superfish of the SC solenoid with old and new designs

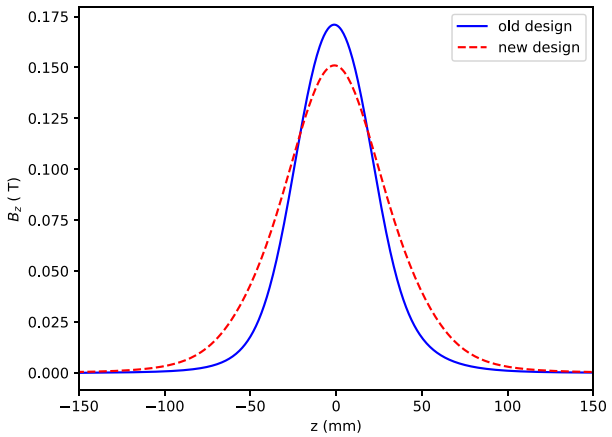

(a)

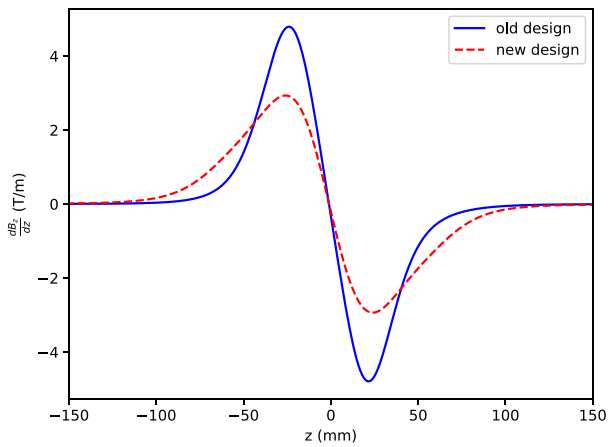

(b)

Fig. 3 (Color online) Comparison between the **a** normalized longitudinal magnetic field and **b** its first derivative for the new and old SC solenoid designs at the same magnetic field integration

entrance, the beam exhibited zero emittance with a Gaussian transverse distribution profile. The magnetic field integral B_z^2 was identical for both designs at $1.19 \times 10^{-3} \mathrm{T}^2 \cdot \mathrm{m}$. The maximum magnetic fields were 0.171 and 0.151 T for the old and new designs, respectively. The integration of the B_z first derivative square was 1.14 $\mathrm{T}^2 \cdot m^{-1}$ for the old design and 0.62 $\mathrm{T}^2 \cdot m^{-1}$ for the new design.

Figure 4 shows the spherical aberration emittance at the solenoid exit for both designs. The new design demonstrated a marked improvement, with the fourth power fitting coefficient being approximately half that of the original design. The coefficient was reduced by approximately 47%, from 0.0061 $\mathrm{mm}^{-3} \cdot$ mrad to 0.0033 $\mathrm{mm}^{-3} \cdot$ mrad. For a 600 pC beam with a Gaussian transverse distribution profile and 4.25 mm RMS size at the solenoid position, the transverse projected emittance at 2.62 m from the cathode decreased from 5.458 mm · mrad with the old design SC solenoid to 4.768 mm · mrad with the new design SC solenoid at the same focal strength. Additionally, when the solenoid is not perfectly aligned, the newly designed SC solenoid will exhibit superior behavior. For instance, if the alignment has a 1 mm offset in the x-direction, the transverse projected emittance will decrease from 5.814 mm · mrad to 4.902 mm. mrad. The average slice emittance decreases by approximately 25%.

4 Measurement setup

Multipole components arise when an offset or tilt exists between the magnetic field axis of the solenoid and its mechanical axis. Misalignments of this type can cause multipole components such as quadrupole or sextupole components to appear. These multipole components distort the beam profile and increase the transverse emittance, thereby degrading the overall beam quality. Identifying and correcting these misalignments are crucial for optimizing the solenoid performance.

Figure 5 shows a photograph of the magnetic field measurement system. The 3D coordinate measurements and mechanical alignment of the solenoid were performed using a Quantum Max metrology tool (mechanical measuring arm) from FARO. This arm was also employed to establish the transverse coordinate origin and ensure proper alignment of the longitudinal axis. Before sealing the cryomodule, this tool was used to determine the mechanical axis of the module and solenoid position relative to the large front side flange of the cryomodule, which served as the reference plane.

The magnetic field was mapped using three motorized linear stages enabling precise three-axis movements. The z-direction stage had a travel range of 0 to 270 mm. Figure 6

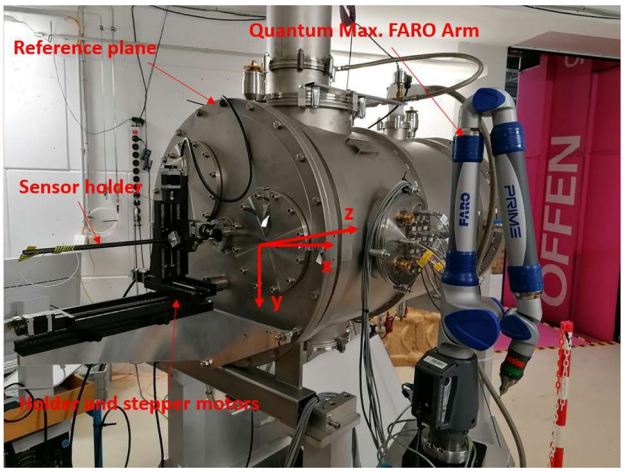

Fig. 5 (Color online) SC solenoid measurement system

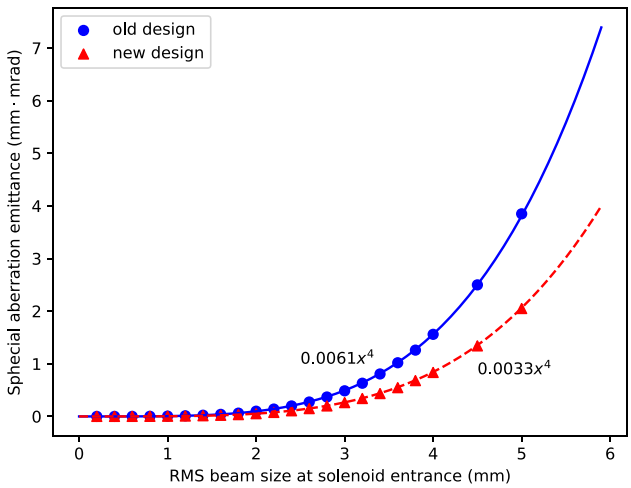

Fig. 4 (Color online) Effect of spherical aberrations

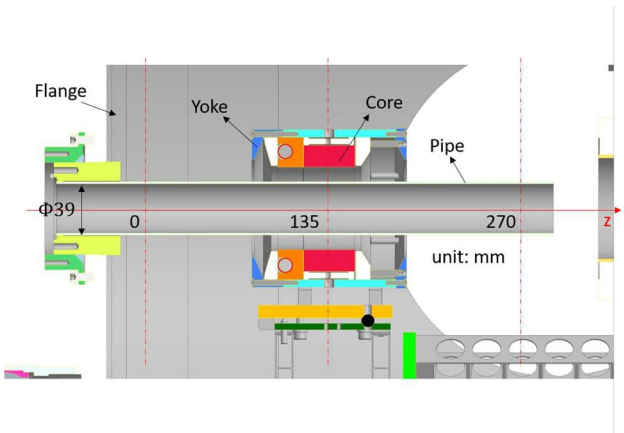

Fig. 6 (Color online) Setup of cryomodule with SC solenoid, tube, and coordinate system

illustrates the installation of the SC solenoid in the cryomodule. The core, fixed by an aluminum support frame, was placed 135 mm away from the original measurement point. The beam pipe diameter was 39 mm. The z-direction stage had a travel range of 0 to 270 mm.

Magnetic field measurements were taken using two Hall sensors. The first sensor (SENIS AG) was employed to measure all three components of the magnetic field. It operates within a range of −200 to 200 mT, and the resolution is 0.001 mT. The active area of this 3D probe measures 150 μm × 150 μm with a thickness of 50 μ m. To ensure the precise alignment and protection of the probes during field mapping, a custom holder was designed (see Fig. 7a). The second was a Magnet-Physik GmbH probe that measures the longitudinal magnetic field component in the range of 3 mT to 3 T (see Fig. 7b).

For the 1D axial probe, measurements of the longitudinal magnetic field component were obtained over a distance of 0 to 270 mm along the mechanical axis of the solenoid, with a step size of 5 mm.

The 3D probe was used to map the transverse magnetic field components over a 12 mm × 11 mm area in the horizontal and vertical directions (see Fig. 8). The center point was the original rectangular point. The step sizes were set to

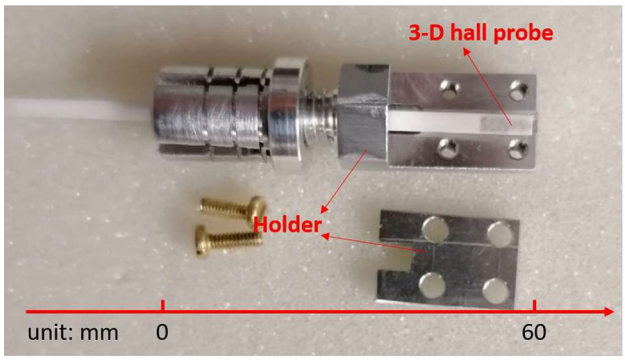

(a)

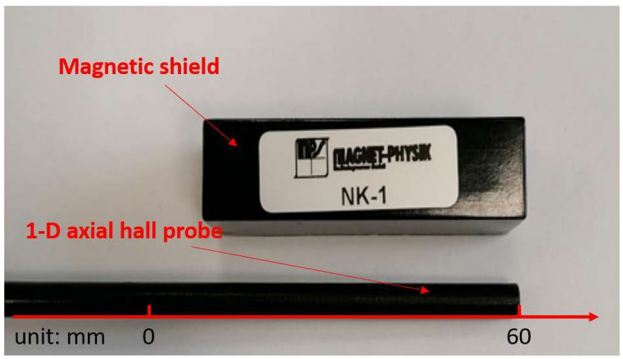

(b)

Fig. 7 (Color online) **a** 3D Hall sensor and **b** 1D Hall sensor

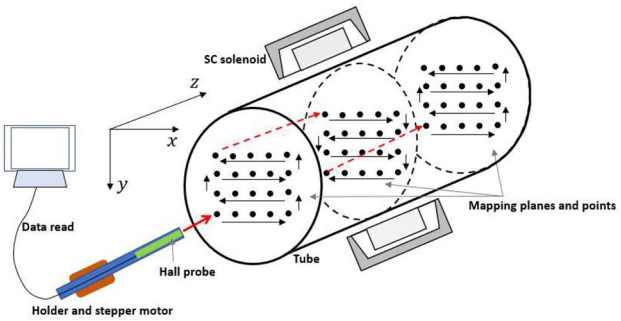

Fig. 8 (Color online) SC solenoid field mapping

1 mm in the x- and y-directions and 5 mm in the z-direction. Each measurement plane required approximately 4.5 min.

5 Field measurement results

The longitudinal field B_z along the solenoid axis was measured using the 1D Hall probe, which was selected for its ease of data processing, allowing for a more efficient and accurate analysis compared with other methods. Owing to the dominance of the longitudinal field over the weaker transverse components, any minor misalignment between the measurement and solenoid axes was considered negligible.

Figure 9a shows the measured longitudinal field profile B_z for currents ranging from 1 A to 8 A. Figure 9b compares the measured data with the computed field profile, revealing excellent agreement between the two.

As anticipated from the behavior of the solenoid, the maximum value of B_z exhibited a linear increase with the solenoid current and the slope coefficient was 35.23 ± 0.02 mT/A, as shown in Fig. 10a. The effective magnetic length was determined as 50.990 mm with a measurement uncertainty of ± 0.068 mm. The results for different currents, which demonstrate a consistent relationship between the field strength and current, are shown in Fig. 10b.

5.1 Misalignment measurement

Detailed spatial field distribution mapping was performed to measure the SC solenoid field accurately, as shown in Fig. 8. The 3D Hall probe was used for these measurements, with the maximum current limited to 5 A owing to the range constraints of the probe. To account for the influence of background magnetic fields, preliminary mapping was conducted at a current of 0 A. These background readings were subsequently subtracted from the standard field measurements before the numerical analysis.

The data analysis involved determining the extrema coordinates (maximum values outside and minimum values inside the solenoid) for each measurement plane using

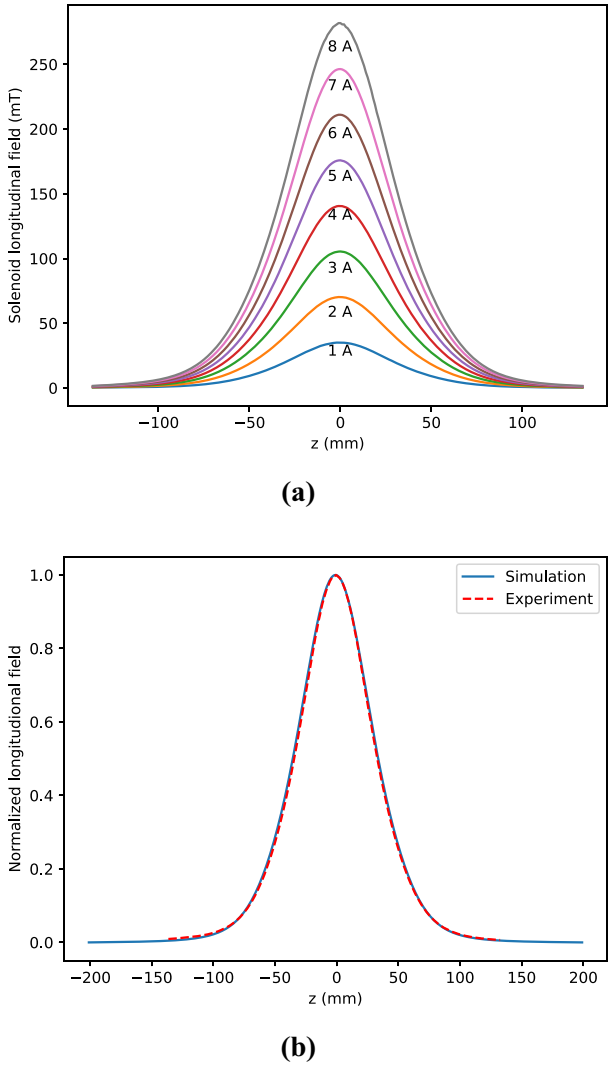

Fig. 9 (Color online) Longitudinal field on the axis of SC solenoid

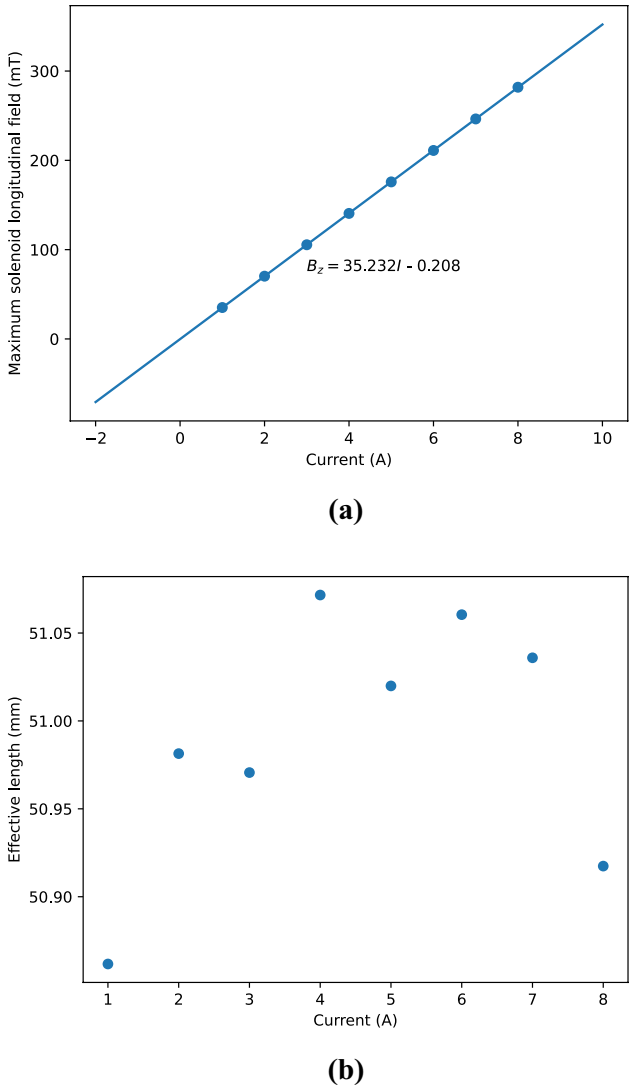

Fig. 10 (Color online) Maximum longitudinal field on the axis and effective length versus current

a parabolic fitting method. Linear regression was applied to the center point coordinates in the z-direction at both the solenoid entrance and exit, yielding two straight lines. The tilt and offset of the solenoid field axis were calculated by averaging the results of these two lines. The SC solenoid offset was 2.27 ± 0.20 mm in the horizontal direction and -0.51 ± 0.02 mm in the vertical direction. The tilts were 7.86 ± 0.87 mrad in the horizontal plane and -23.07 ± 1.23 mrad in the vertical plane.

Although the offset of the solenoid can be adjusted by repositioning the $x - y$ stage during SRF gun operation, any tilt in the field axis of the solenoid, once established, cannot be corrected later. Potential sources of misalignment between the magnetic field axis of the solenoid and the measurement axis include discrepancies between the solenoid magnetic field axis and mechanical axis, inaccuracies in the solenoid alignment relative to the reference plane, errors in the measurement coordinate system, and data analysis inaccuracies. Furthermore, magnetic hysteresis in the solenoid or adjacent components, as well as thermal contraction effects during cooldown to 4.5 K, may contribute to alignment deviations.

5.2 Multipole modes

The multipole component analysis focused on the transverse magnetic field, measured using the 3D Hall probe, to characterize higher-order magnetic field structures accurately. Before performing a detailed evaluation of the field mapping data, the background magnetic field measurements were subtracted to remove any residual environmental noise or baseline offsets and to ensure the accuracy of the subsequent analysis.

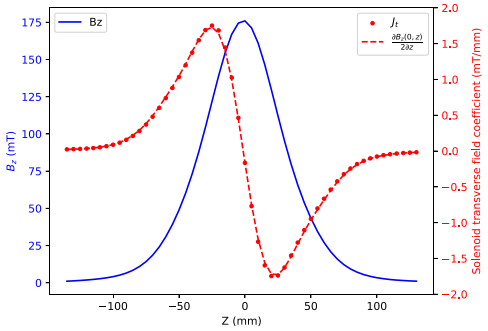

(a)

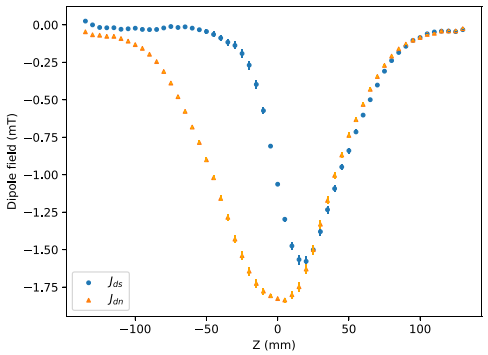

(b)

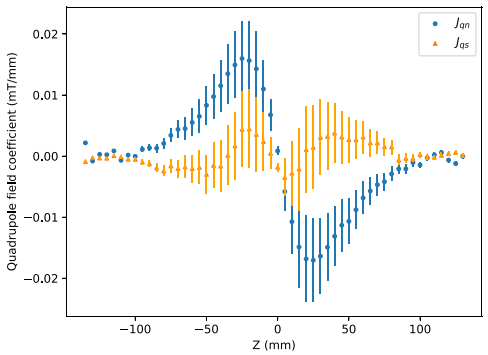

(c)

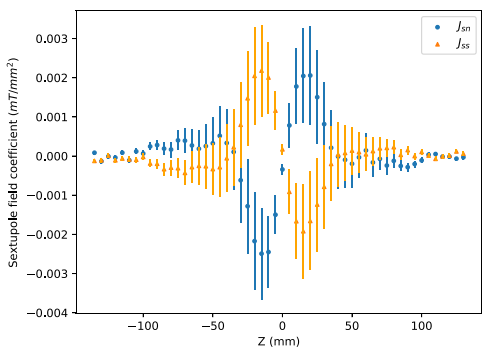

(d)

Fig. 11 (Color online) SC solenoid transverse field multipole coefficients. **a** Solenoid radial field distribution. **b** Normal and skew dipole component distribution. **c** Normal and skew quadrupole component distribution. **d** Normal and skew sextupole component distribution

The primary objective of the data processing was to compute the coefficients of the multipole modes that describe the strength and nature of the higher-order components of the magnetic field. These coefficients were calculated based on the measured transverse fields for each plane, following the formulation provided in Eq. 7. Accurate center coordinates, which are essential for determining the symmetry and alignment of the multipole modes, were obtained from previous axis measurements.

In the final step, a fitting procedure was applied to the data for each measurement plane, allowing for the extraction of multipole coefficients that characterize the transverse components of the field. For example, Fig. 11 shows the multipole component distribution of the SC solenoid at 5 A.

In Fig. 11a, the solenoid radial field coefficient J_t obtained from the measurement is compared with the corresponding curve derived from the first derivative of the measured B_z on the axis. The consistency between these two results confirms the validity and accuracy of the measurement process.

Figure 11b illustrates two components of the dipole field parasite in the solenoid. The normal mode exhibited symmetry around the center of the solenoid, whereas the skew mode was asymmetric, indicating the presence of minor field imperfections.

The overall dipole field, which accounted for both the normal and skew modes, can be described by the following equation, which characterizes the complete dipole structure of the field:

$$\mathbf{B}_{\mathrm{d}} = \mathbf{B}_{\mathrm{dn}} + \mathbf{B}_{\mathrm{ds}} = -J_{\mathrm{ds}}\mathbf{e}_{\mathbf{x}} + J_{\mathrm{dn}}\mathbf{e}_{\mathbf{y}}. \tag{21}$$

By integrating the transverse field components along the z-axis, the resulting values determined the magnitude and direction of the dipole kick exerted on the beam. This kick influenced the trajectory of the beam as it passed through the solenoid, with both the strength and orientation depending on the transverse field distribution.

In Fig. 12a, the magnitude and phase of the dipole field are shown as functions of the longitudinal position z, and a distinct phase change is observed at the central plane of the solenoid, which may indicate field reversal or changes in field symmetry across the solenoid.

As shown in Fig. 12b, the integration of the dipole field strength was proportional to the current, confirming the proportional relationship between the current and transverse dipole field. This linearity is key to predicting the beam-steering effects caused by the solenoid under varying operational conditions.

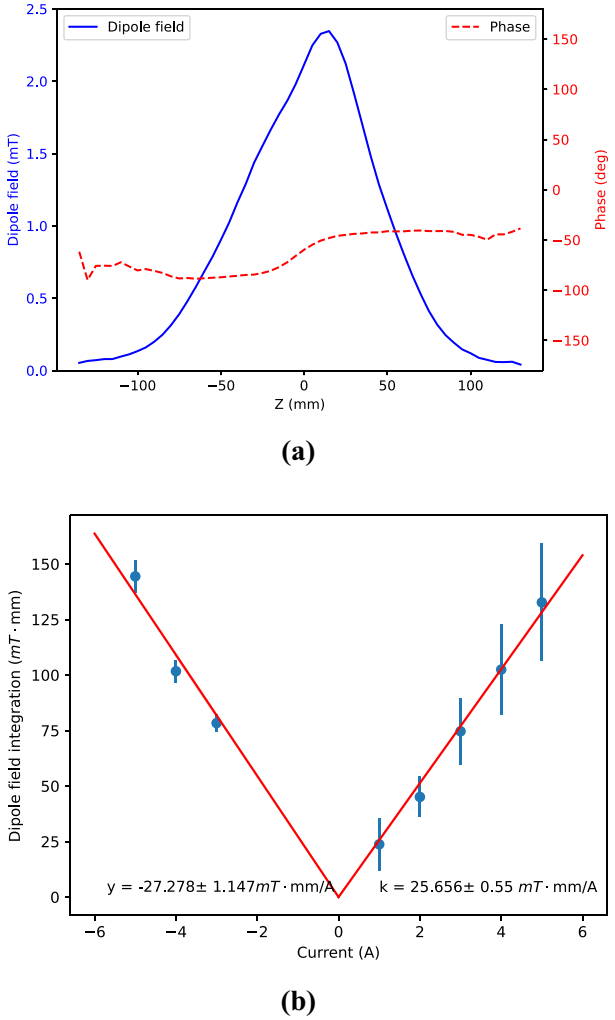

Fig. 12 (Color online) **a** Dipole mode amplitude and phase distribution @ 5 A. **b** Integration of dipole mode strength vs. solenoid current

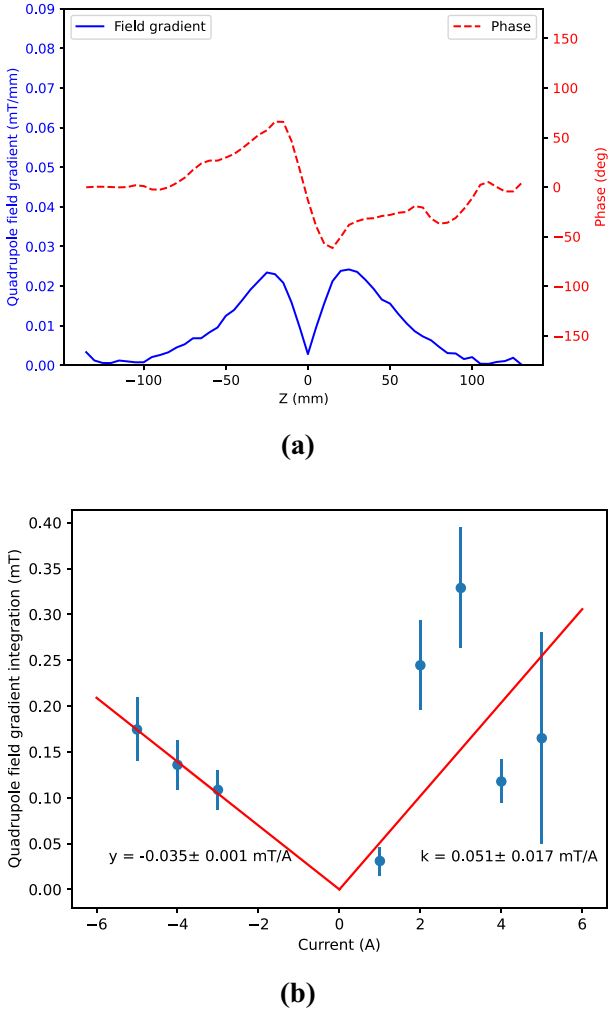

Fig. 13 (Color online) **a** Quadrupole field gradient and phase distribution @ 5 A. **b** Integrated quadrupole gradient with current

The parasitic quadrupole component shown in Fig. 11c demonstrates antisymmetry about the central plane of the solenoid, with the dominant normal quadrupole mode reversing its sign across the center. Because of this antisymmetry, the integrated quadrupole gradient derived from the z-integration of the quadrupole components was almost zero. This suggests that, in the absence of other effects, the net focus or defocus from the quadrupole field is minimal over the entire solenoid.

However, the Larmor rotation of the coordinate frame of the beam as it traverses the solenoid can cause coupling between the transverse motions. This rotation may lead to observable effects on the beam, even when the integrated quadrupole field is negligible. To evaluate the impact of the total quadrupole field on the beam accurately, both the normal and skew components must be combined, as represented by the following equation:

$$\begin{aligned}\mathbf{B}_{\mathrm{q}} = \mathbf{B}_{\mathrm{qn}} + \mathbf{B}_{\mathrm{qs}} = (J_{\mathrm{qn}}y - J_{\mathrm{qs}}x)\mathbf{e}_{\mathbf{x}} \\ +(J_{\mathrm{qn}}x + J_{\mathrm{qs}}y)\mathbf{e}_{\mathbf{y}}.\end{aligned} \tag{22}$$

Figure 13a shows the polar representation of the quadrupole gradient, displaying both its magnitude and phase with the longitudinal position z. This representation provides insight into the spatial variation and orientation of the quadrupole field components.

In Fig. 13b, the integrated quadrupole gradient is plotted against the solenoid current, revealing the linear dependence of the field strength on the current. Notably, the slopes of the currents with different signs in Fig. 13b differ only slightly. This discrepancy may be attributed to systematic measurement errors, such as probe misalignment, noise in the data acquisition system, or nonideal calibration of the Hall probes.

To mitigate the effects of the parasitic quadrupole field generated by the SC solenoid, a set of correctors comprising one normal quadrupole and one skew quadrupole were strategically placed 437 mm downstream of the solenoid center in the SRF gun beamline. Each corrector had an effective length of 0.0672 m and provided a gradient of 12 mT/m/A.

When operating SRF Gun-III at an accelerating gradient of 12 MV/m, corresponding to a kinetic energy of 6 MeV, the SC solenoid current was set to 6 A to focus the beam and mitigate the growth of the transverse emittance. Consequently, the solenoid induced an integrated quadrupole field gradient of 0.192 mT with a peak value of 48 mT/m over an effective length of 4 mm.

Owing to the uncertainty in the phase of the parasitic quadrupole field, simulations using ASTRA were performed to analyze its impact on the beam dynamics. Under specific phase conditions, the parasitic quadrupole field could reduce the initial beam emittance, potentially compensating for the spherical aberration of the solenoid. However, this effect was contingent on the precise phase alignment.

In most cases, the parasitic quadrupole field exacerbated transverse emittance growth, making it critical to cancel this effect using correction techniques. Assuming the worst-case scenario in which the quadrupole field phase is misaligned by 45.8°, as shown in Fig. 14, and applying a current of 1 A to the corrector, Fig. 15 demonstrates that the emittance oscillation was significantly reduced. The simulation results confirm that the correctors, when properly adjusted, effectively nullify the influence of the parasitic quadrupole field of the solenoid, thus preventing additional emittance growth.

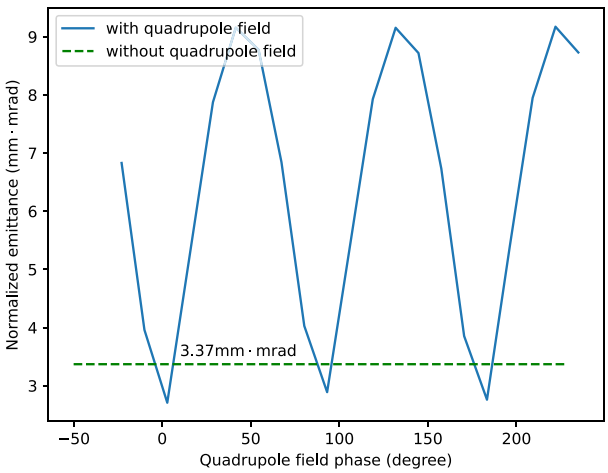

Fig. 14 (Color online) Normalized emittance change with quadrupole field rotation angle in simulation. The beam with a 500 pC bunch charge had 6 MeV of kinetic energy. We ignored the space charge when considering the quadrupole field in the solenoid. The solenoid current was 6 A and located 55 mm downstream of the cathode. The component focal strength of the parasitic quadrupole was 2.21 m^{-2}, and its effective length was 4 mm

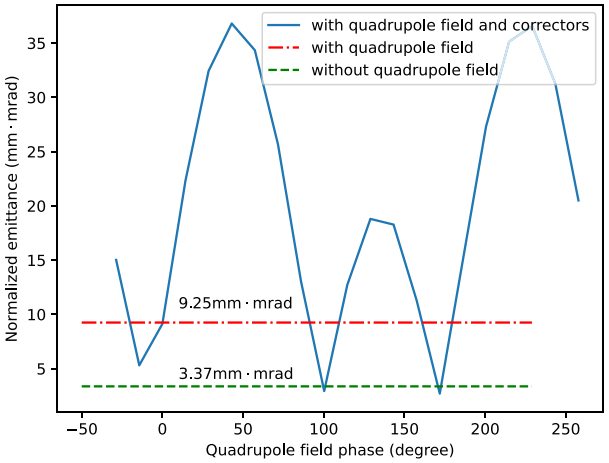

Fig. 15 (Color online) Normalized emittance versus corrector rotation angle

$$\mathbf{B}_s = \mathbf{B}_{sn} + \mathbf{B}_{ss} = \left[J_{sn}xy - \frac{1}{2}J_{ss}(x^2 - y^2)\right]\mathbf{e_x} + \left[\frac{1}{2}J_{sn}(x^2 - y^2) + J_{ss}xy\right]\mathbf{e_y}. \tag{23}$$

The sextupole field characteristics are illustrated in Fig. 16a, which shows the sextupole field coefficient and its phase along the longitudinal direction at a solenoid current of 5 A. The amplitude of the sextupole field was approximately symmetric with respect to the original point (the solenoid center), with maximum values of approximately 0.0025 mT/mm^2 occurring in the mirror planes. Additionally, the phase underwent significant changes near the center, with the maximum and minimum strength values observed at these mirror planes. At the edges of the solenoid, the phase measurement became unstable because of the small magnitude of the sextupole coefficient, which resulted in significant noise interference and limited accurate fitting. Although the z-integral of the sextupole field coefficient is expected to be proportional to the solenoid current, the measured results do not align with this expectation, as shown in Fig. 16b. This discrepancy likely arose because the sextupole component was outside the accuracy range of the measurement method.

We evaluated the influence of the sextupole field on the transverse emittance in the context of SRF Gun-III using a bunch charge of 500 pC. The simulations revealed that the beam RMS size at the solenoid position was approximately 4 mm. When the solenoid current was fixed at 6 A, the sextupole field exhibited an amplitude of approximately 0.005 mT/mm^2 and an effective length of 6 mm. For a beam characterized by a lateral Gaussian distribution of the transverse profile, the additional normalized emittance introduced by the sextupole field was approximately 0.9 mm · mrad. By contrast, for a uniform beam distribution, the additional

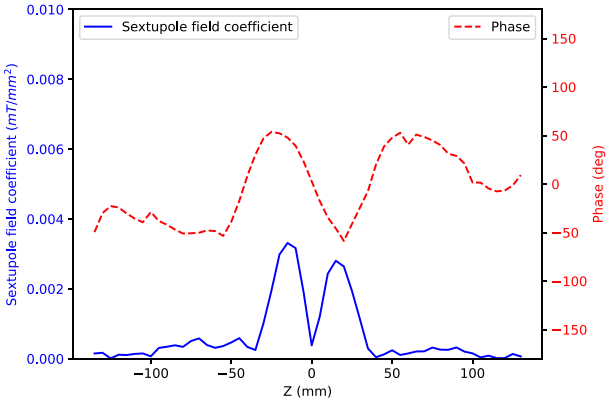

(a)

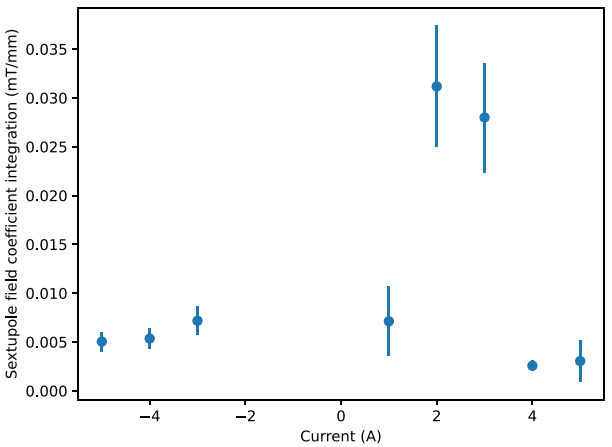

(b)

Fig. 16 (Color online) **a** Sextupole field coefficient and phase distribution @ 5 A. **b** Integration of sextupole field coefficient versus solenoid current

emittance was reduced to approximately 0.52 mm · mrad. Consequently, based on Eq. 20, the overall effect of the sextupole field on the transverse emittance was estimated to be approximately 20%.

5.3 Analysis of error sources

The measurement uncertainties associated with the SC solenoid stem from four primary sources: 1. Mechanical alignment of the Hall probe: Inaccuracies in the mechanical alignment of the Hall probe can lead to erroneous magnetic field measurements. Even slight misalignments can result in significant discrepancies in the recorded data. 2. Degaussing of the yoke: Incomplete or imperfect degaussing of the yoke can introduce residual magnetic fields that may affect the accuracy of the measurements by masking or distorting the intended signal. 3. Intrinsic errors of the Hall probe: Each Hall probe has inherent measurement errors owing to its construction and operating principles, which can contribute to the overall uncertainty in the magnetic field measurements. 4. Data fitting errors: Errors introduced during the data fitting process can arise from the mathematical models used, as well as the selection of fitting parameters. These factors can affect the accuracy of the derived magnetic field values.

The field measurements were taken over the course of one week, with each full mapping session requiring approximately 4.5 h. Owing to the limitations in the measurement system, such as the z-axis movement range and initialization procedure, the Hall probe required daily manual realignment with a marker. This manual realignment resulted in a longitudinal position error of less than 0.8 mm and a rotational error of less than 60 mrad. Consequently, the longitudinal field error of the solenoid owing to realignment was estimated to be less than 2%, whereas the uncertainty in the transverse field was less than 6%.

The second source of error arises from incomplete degaussing of the soft iron yoke. Although the background field was recorded, it was not measured prior to each mapping session. Background measurements were taken at three key instances: before the measurement period, immediately prior to increasing the solenoid current to 4 A and then to 5 A, and finally, after measuring the magnetic field at −3 A. As illustrated in Fig. 17, the background field variation along the mechanical axis was approximately 0.125 mT. Although we subtracted this background field before performing the multipole field analysis, its variations introduced additional uncertainties. The average differences in the multipole component integrals were approximately 18.4% for the dipole fields, 30.4% for the quadrupole field gradients, and 21.4% for the sextupole field coefficients.

In terms of the measurement equipment, the active area of the 1D Hall sensor was a circular area with a diameter of 0.4 mm, representing the average over a circular area of 0.126 mm^2. The calibration uncertainty of the 1D hall probe was 0.25% [35]. The core size of the 3D Hall sensor was 0.15 mm × 0.1 mm × 0.15 mm and the measurement precision was better than ±0.1% [36]. Additionally, the intrinsic alignment error of the sensor areas in the 3D Hall sensor was approximately 17.45 mrad, as shown in Fig. 18 [36].

Figure 11 shows that the fitting errors were predominantly associated with the quadrupole field gradient and sextupole field coefficients. By contrast, the average fitting error in the simulations, attributed to the finite grid size, was less than 1%. The observed fitting errors were 2%, 73%, and 90% for

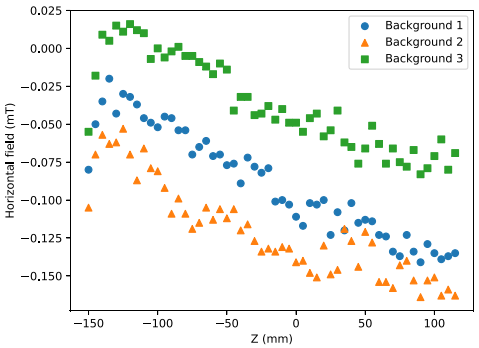

(a)

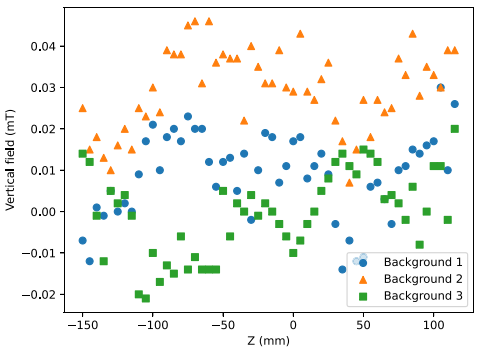

(b)

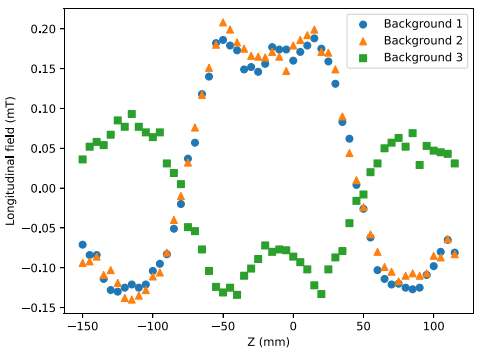

(c)

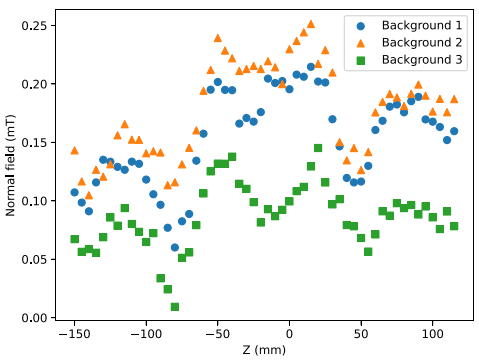

(d)

Fig. 17 (Color online) Background field distribution. **a** Before the whole measurement period; **b** after the measurement of solenoid current with 4 A; **c** before the solenoid current was increased to 5 A; **d** after the measurement of solenoid current with −3 A

the dipole fields, quadrupole field gradients, and sextupole field coefficients, respectively.

The overall fitting error reflects the cumulative impact of these individual errors, underscoring the significant influence of the quadrupole and sextupole components on the accuracy of the multipole field measurements. This highlights the importance of addressing these fitting errors to improve the measurement reliability.

6 Conclusion

We optimized the SC solenoid design to reduce the spherical aberration, with a focus on modifying the geometry and field distribution. The effective length and field strength coefficient, as determined from measurements under an operational current, were found to be in excellent agreement with the simulation results, confirming the accuracy of our solenoid design.

An analysis of the high-order magnetic components, including the quadrupole and sextupole components, was conducted to assess their impact on the beam transverse emittance. Although the formalism fitting method used for multipole component analysis did not yield highly precise results for the reasons discussed in the previous section, it provided valuable insights into the solenoid performance in the beamline and can help to guide further optimization efforts.

The correctors installed in the beamline effectively compensated for the adverse impact of the quadrupole field on the beam transverse emittance. However, the sextupole component remains a critical factor in optimizing the future performance of the solenoid because it introduces nonlinear field effects that significantly impact the beam quality.

A practical solution to mitigate the effects of the sextupole component is to install a sextupole corrector in close proximity to the SC solenoid. This would allow for fine-tuning of the higher-order field components and enhance the overall beam quality. This addition could significantly enhance the performance by further mitigating sextupole effects.

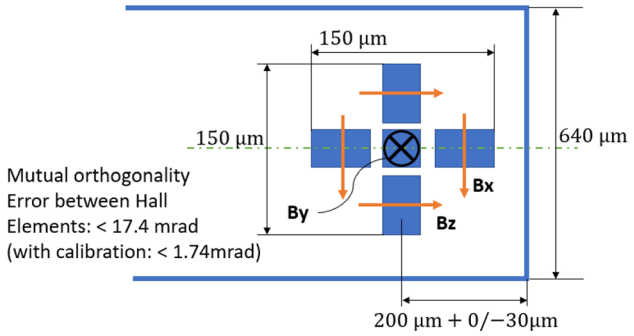

Fig. 18 (Color online) 3D sensor alignment

Acknowledgements We would like to thank Dr. Houjun Qian from Zhang Jiang Lab, Chinese Academy of Science.

Author Contributions All authors contributed to the study conception and design. Material preparation, data collection and analysis were performed by Shuai Ma, Andre Arnold, Peter Michel, Petr Murcek, Anton Ryzhov, Jana Schaber, Jochen Teichert, and Rong Xiang. The first draft of the manuscript was written by Shuai Ma, and all authors commented on previous versions of the manuscript. All authors read and approved the final manuscript.

Funding Open Access funding enabled and organized by Projekt DEAL.

Data Availability The data that support the findings of this study are openly available in Science Data Bank at https://cstr.cn/31253.11.sciencedb.j00186.00826 and https://www.doi.org/10.57760/sciencedb.j00186.00826.

Declarations

Conflict of interest The authors declare that they have no conflict of interest.

References

1. F. Gabriel, P. Gippner, E. Grosse et al., The Rossendorf radiation source ELBE and its FEL projects. Nucl. Instrum. Methods Phys. Res. Sect. A **161**, 1143–1147 (2000). https://doi.org/10.1016/S0168-583X(99)00909-X
2. P. Michel, ELBE center for high-power radiation sources. J. Large-Scale Res. Facil. **2**, A39 (2016). https://doi.org/10.17815/jlsrf-2-58
3. M. Helm, S. Winnerl, A. Pashkin et al., The Elbe infrared and Thz facility at Helmholtz-Zentrum Dresden-Rossendorf. Eur. Phys. J. Plus **138**, 158 (2023). https://doi.org/10.1140/epjp/s13360-023-03720-z
4. A. Arnold, J. Teichert, Overview on superconducting photoinjectors. Phys. Rev. Accel. Beams **14**, 024801 (2011). https://doi.org/10.1103/PhysRevSTAB.14.024801
5. J. Teichert, A. Arnold, G. Ciovati et al., Successful user operation of a superconducting radio-frequency photoelectron gun with Mg cathodes. Phys. Rev. Accel. Beams **24**, 033401 (2021). https://doi.org/10.1103/PhysRevAccelBeams.24.033401
6. J. Teichert, A. Arnold, H. Büttig et al., Free-electron laser operation with a superconducting radio-frequency photoinjector at ELBE. Nucl. Instrum. Methods Phys. Res. Sect. A **743**, 114 (2014). https://doi.org/10.1016/j.nima.2014.01.006
7. R. Xiang, A. Arnold, J.W. Lewellen, Superconducting radio frequency photoinjectors for CW-XFEL. AIP Conf. Proc. **11**, 1166179 (2023). https://doi.org/10.3389/fphy.2023.1166179
8. R. Xiang, A. Arnold, P. Lu et al., Study of magnisium photocathodes for superconducting rf photoinjectors. *In Proceedings of the 2018 International Particle Accelerator Conference*, Vancouver, Canada (JACoW, Geneva, 2018), p. 4142. https://doi.org/10.18429/JACoW-IPAC2018-THPMF039
9. J. Schaber, R. Xiang, W. Gaponik, Review of photocathodes for electron beam sources in particle accelerators. J. Mater. Chem. C **11**, 3162–3179 (2023). https://doi.org/10.1039/D2TC03729G
10. P. Lu, Optimization of an SRF gun for high bunch charge applications at ELBE, Ph.D. thesis, TU Dresden (2017). https://api.semanticscholar.org/CorpusID:116101949
11. J. Klug, E. Altstadt, C. Beckert et al., Development of a neutron time-of-flight source at the ELBE accelerator. Nucl. Instrum. Methods Phys. Res., Sect. A **577**, 641 (2007). https://doi.org/10.1016/j.nima.2007.04.132
12. X.J. Wang, P. Musumeci, Report of the basic energy sciences workshop on the future of electron sources. SLAC National Accelerator Laboratory (2016). https://api.semanticscholar.org/CorpusID:226949223
13. B. Green, S. Kovalev, V. Asgekar et al., High-field high-repetition-rate sources for the coherent THz control of matter. Sci. Rep. **6**, 22256 (2016). https://doi.org/10.1038/srep22256
14. A. Jochmann, A. Irman, M. Bussmann et al., High resolution energy-angle correlation measurement of hard X rays from laser-Thomson backscattering. Phys. Rev. Lett. **111**, 114803 (2013). https://doi.org/10.1103/PhysRevLett.111.114803
15. H. Vennekate, A. Arnold, P. Lu et al., Emittance compensation schemes for a superconducting rf injector. Phys. Rev. Accel. Beams **21**, 093403 (2018). https://doi.org/10.1103/PhysRevAccelBeams.21.093403
16. H. Vennekate, Emittance compensation for SRF Photoinjectors, Ph.D. thesis, TU Dresden (2017). https://www.hzdr.de/publications/Publ-25925
17. M.E. Schulze, Spherical aberrations-final focus and solenoid scans. Los Alamos National Lab (LANL), Los Alamos. NM (United States) (2020). https://doi.org/10.2172/1635496
18. D.H. Dowell, Sources of emittance in RF Photocathode Injectors: Intrinsic emittance, space charge forces due to non-uniformities, RF and solenoid effects, arXiv:**1610**.01242 (2016). https://api.semanticscholar.org/CorpusID:119211195
19. S. Ma, A. Arnold, P. Michel et al., The application of encoder-decoder neural networks in high accuracy and efficiency slit-scan emittance measurements. Nucl. Instrum. Methods Phys. Res. Sect. A **1050**, 168125 (2023). https://doi.org/10.1016/j.nima.2023.168125
20. L.M. Zheng, J.H. Shao, Y.C. Du et al., Experimental demonstration of the correction of coupled transverse dynamics aberration in

an rf photoinjector. Phys. Rev. Accel. Beams **22**, 072825 (2019). https://doi.org/10.1103/PhysRevAccelBeams.22.072805
21. E. Prat, P. Dijkstal, M. Aiba et al., Generation and characterization of intense ultralow-emittance electron beams for compact x-ray free-electron lasers. Phys. Rev. Lett. **123**, 234801 (2019). https://doi.org/10.1103/PhysRevLett.123.234801
22. M. Altarelli, The European X-ray free-electron laser facility in Hamburg. Nucl. Instrum. Methods Phys. Res. Sect. B **269**, 2845–2849 (2021). https://doi.org/10.1016/j.nimb.2011.04.034
23. E.A. Seddon, J.A. Clarke, D.J. Dunning et al., Short-wavelength free-electron laser sources and science: a review. Rep. Prog. Phys. **80**, 115901 (2017). https://doi.org/10.1088/1361-6633/aa7cca
24. H. Vennekate, A. Arnold, P. Lu et al., Building the third SRF gun at HZDR, RF and solenoid effects, In *Proceedings of the 2017 International Beam Instrumentation Conference (IBIC'17), Geneva, Switzerland (JACoW, Geneva, 2017)*, p. 98. https://doi.org/10.18429/JACoW-IPAC2021-WEXC03
25. K. Zhou, A. Arnold, P. Li et al., Preliminary ceometry optimization of a 3.5-Cell SRF Gun Cavity at ELBE based on beam dynamics, In *Proceedings of the 2019 Free Electron Laser Conference (FEL'19)*, Hamburg, Germany (JACoW, Geneva, 2019), p. 374. https://doi.org/10.18429/JACoW-SRF2019-THP082
26. D. Arbelaez, A. Madur, L. M. Lipton et al., Magnetic alignment of pulsed solenoids using the pulsed wire method. In *Proceedings of the 2011 International Particle Accelerator Conference*, New York, USA (JACoW, Geneva, 2011), p. 2087–2089. https://escholarship.org/uc/item/73x346g7
27. P. Arpaia, M. Buzio, J.J.G. Perez et al., Magnetic field measurements on small magnets by vibrating wire systems, 2011 IEEE International Instrumentation and Measurement Technology Conference, IEEE, 1–4 (2011). https://doi.org/10.1109/IMTC.2011.5944265
28. P. Arpaia, C. Petrone, S. Russenschuck et al., Vibrating-wire measurement method for centering and alignment of solenoids. J. Instrum. **8**, P11006 (2013). https://doi.org/10.1088/1748-0221/8/11/P11006
29. H. Wiedemann, Particle accelerator physics. Springer Nature (2015). https://doi.org/10.1007/978-3-319-18317-6
30. D.H. Dowell, F. Zhou, J. Schmerge, Exact cancellation of emittance growth due to coupled transverse dynamics in solenoids and RF couplers. Phys. Rev. Accel. Beams **21**(1), 010101 (2018). https://doi.org/10.1103/PhysRevAccelBeams.21.010101
31. K. Flöttmann, ASTRA: A space charge tracking algorithm, manual, version 3, 2011, update April 2014. https://www.desy.de
32. Q. Jiang, S.D. Anderson, D. Dowell et al., Beam Dynamics Simulation of the Solenoid Sextupole Error in the LCLS-II Injector, SLAC National Accelerator Lab., Menlo Park, CA (United States) (2018). https://doi.org/10.18429/JACoW-IPAC2018-THPMF085
33. D.H. Dowell, Correcting emittance growth due to stray sextupole fields. arXiv preprint arXiv:1810.00086 (2018)
34. J.H. Billen, L.M. Young, POISSON/SUPERFISH on PC compatibles. In Proceedings of International Conference on Particle Accelerators, Washington, DC, USA **2**, 790–792 (1993). https://doi.org/10.1109/PAC.1993.308773
35. Magnet-Physik Dr. Steingroever GmbH. USB Hall probes. Köln (2008). https://www.magnet-physik.de/
36. SENIS magnetic & current measurement. Fully integrated 3-Axis Hall Probe HL, HM, HS. SENIS AG, Switzerland (2017). https://www.senis.swiss/magnetometers/hall-probes/